Single-cell resolution functional networks during sleep are segregated into spatially intermixed modules

Daiki Kiyooka[1†], Ikumi Oomoto[2†], Jun Kitazono[1], Midori Kobayashi[2], Chie Matsubara[2], Kenta Kobayashi[3], Masanori Murayama[2‡*], and Masafumi Oizumi[1‡*]

[1]Department of General Systems Studies, Graduate School of Arts and Sciences, The University of Tokyo, 3-8-1 Komaba, Meguro-ku, Tokyo 153-8902, Japan
[2]Center for Brain Science, RIKEN, 2-1 Hirosawa, Wako-shi, Saitama 351-0198, Japan
[3]Section of Viral Vector Development, National Institute for Physiological Sciences, 38 Nishigonaka, Myodaiji-cho, Okazakishi, Aichi 444-8585, Japan
†These authors contributed equally to this work.
‡These authors contributed equally to this work.
∗ Corresponding authors.
Emails: `masanori.murayama@riken.jp`; `c-oizumi@g.ecc.u-tokyo.ac.jp`

Abstract

The neural mechanisms responsible for the reduction of consciousness during sleep remain elusive. Previous studies investigating macro/mesoscale neural data have suggested that functional networks are segregated into spatially localized modules, and that these modules are more segregated during sleep than during wakefulness. However, large-scale single-cell resolution functional networks remain largely unexplored. Here, we simultaneously recorded the activities of up to 10,000 cortical neurons from multiple brain regions in mice during wakefulness and sleep using a fast, single-cell resolution, and wide-field-of-view two-photon calcium imaging technique. We examined how networks were integrated or segregated between brain states in terms of modularity and spatial distribution in the cortex. We found that modularity during non-rapid eye movement sleep was higher than that during wakefulness, indicating a more segregated network. However, these modules were not spatially localized but rather intermixed across regions in both states. Our results provide novel insights into differences in the cellular-scale organization of functional networks during altered states of consciousness.

Introduction

The process by which consciousness diminishes during sleep remains elusive in neuroscience. Prevailing theories of consciousness propose that the brain's ability to integrate information is an indispensable prerequisite for consciousness, given the unified nature of the conscious experience [1–4]. Such information integration is enabled by an intricate brain network facilitated by neuronal interactions at the microscale and the interplay of brain regions at the mesoscale. Thus, from a network perspective, it is crucial to compare and contrast to what extent and how (i.e., spatial organization) the brain network is integrated at both micro- and mesoscale levels during states of wakefulness and sleep [5–7]. Such network-level understanding is pivotal for elucidating the neural underpinnings of reduced consciousness during sleep.

Current empirical findings from studies using macro/mesoscale neural recordings, such as functional MRI (fMRI) and electroencephalography (EEG), suggest that functional networks are more segregated

during non-rapid eye movement (NREM) sleep than during wakefulness [8–15]; that is, interactions across brain regions are diminished. For example, a perturbational approach using transcranial magnetic stimulation (TMS) has shown that TMS-evoked EEG potentials do not propagate across brain regions during NREM sleep, but do so during wakefulness, implying a breakdown of cortical effective connectivity during NREM sleep [12]. Another approach, using a graph-theoretic measure called modularity, has shown that functional networks are more segregated into spatially localized modules during NREM sleep than during wakefulness [9, 14].

While many past studies have focused on the macro/mesoscale properties of networks [9, 11, 14–26], a crucial aspect that has not been adequately explored is understanding the brain network as a multiscale entity and relating network properties at one spatial scale to those at another [27, 28]. Among different spatial scales, it is evidently important to gain insight into the brain network at the cellular-scale because (1) the neuron is one of the most elementary components of the network [29] and (2) based on single-cell resolution data, it is possible to search for the most relevant functional units, regardless of whether they are single neurons or groups of neurons [30, 31]. On the other hand, it is impossible to search for the most relevant functional unit using only macroscale data without single-cell resolution data. Since the most relevant functional units have been largely unknown for explaining the alteration of levels of consciousness during sleep [4, 32–34], it is also a vital step in consciousness research to investigate more on cellular-resolution networks and reveal the relationship between the network properties at the cellular-scale and those at the macro/mesoscale. Although a few studies have investigated single-cell resolution functional networks, these studies analyzed data from a limited brain area [35–39] or a limited number of neurons [40–42] because of their narrow recording sites. Therefore, little is currently known about cellular-resolution functional networks across multimodal brain regions.

To uncover the differences in cellular-scale network structures depending on the brain state, we used a fast, single-cell resolution, and wide-field-of-view (FOV) two-photon laser scanning microscope, FASHIO-2PM, recently developed by our group [43, 44]. Using this innovative calcium imaging technique, we recorded the activity of up to 10,000 neurons at 7.65 Hz sampling rate from each mouse during both wakefulness and sleep. The FOV spanning a contiguous 3 mm $\times$ 3 mm area encompasses multiple cortical regions, including the somatosensory, motor, and other cortices, enabling the exploration of cellular networks over expansive brain areas during both wakefulness and sleep in mice for the first time.

Using a large dataset obtained from FASHIO-2PM, we first investigate how functional networks composed of modules are segregated or integrated during wakefulness and NREM sleep. Second, we investigate whether the modules are localized to specific areas or scattered across the entire FOV. Third, we investigate specific neurons that connect different modules (i.e., connector hubs) or many other neurons within a module (i.e., provincial hubs) (Fig. 1) [45, 46]. Addressing these questions will provide an understanding of single-cell resolution functional networks during wakefulness and NREM sleep.

We show that "modularity," a graph-theoretic measure that quantifies the extent to which a network can be segregated into non-overlapping modules [47, 48], is higher during NREM sleep than during wakefulness. This suggests that, similar to macro/mesoscale functional networks, cellular-scale functional networks are more segregated during NREM sleep than during wakefulness. However, we show that neurons belonging to the same module are spatially scattered across regions during both wakefulness and NREM sleep. We also demonstrate that the hubs are spatially scattered. These results suggest that the cellular-resolution functional networks are spatially intermixed. This is different from previous findings in macro/mesoscale functional network analyses because our results suggest that there are functional connections across brain regions during both wakefulness and NREM sleep. This nuanced perspective challenges the traditional view that functional networks are localized in segregated modules during sleep, thereby reshaping our understanding of functional networks during NREM sleep.

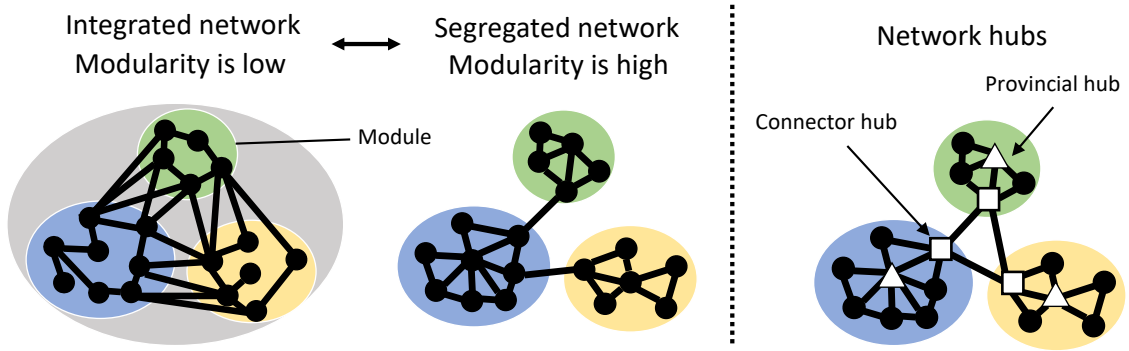

Figure 1: Schematic illustration of the concept of modularity and hubs.

Results

Fast, cell-resolution, contiguous-wide two-photon calcium imaging across multi-modal cortical areas during wakefulness and sleep

To record the large-scale neuronal activity in sleeping mice, we used a fast and wide-field two-photon microscope (FASHIO-2PM) [43, 44]. The field-of-view spanning a contiguous 3 mm $\times$ 3 mm area allowed us to record multiple brain regions in cortical layer 2/3, including the somatosensory and motor cortices (Fig. 2). To determine the sleep stages in mice, we simultaneously recorded electromyography (EMG) potentials from neck muscles and EEG signals from screw electrodes placed on the lateral secondary visual area (V2L) in the same hemisphere used for imaging (Fig. 2b) (see Materials and Methods). Simultaneous recordings of neural calcium signals, EEG, and EMG were performed during the light phase (Zeitgeber time 3–5). Four sleep states were determined by post-hoc analysis of the EEG and EMG: wakefulness, non-REM sleep, REM sleep, and quiet wake. As REM sleep and quiet wake were rare ($<$ 5% of the recording period; Supplementary Fig. 1), we focused on wakefulness and NREM sleep for subsequent analysis. For each region of interest (ROI), we examined whether there were differences in firing characteristics during wakefulness and NREM, and found that firing frequency and amplitude tended to be higher during wakefulness (Supplementary Fig. 1).

Framework for investigating network structure

We focused on the structure of functional networks during wakefulness and NREM sleep, particularly in terms of network segregation (or integration). Modularity is used as a measure to quantify the degree of network segregation. It quantifies the extent to which a network can be divided into non-overlapping "modules," where neurons within the same modules are densely connected but those with different modules are sparsely connected. The lower the modularity, the more integrated the network, whereas the higher the modularity, the more segregated the network (Fig. 1) [49].

There were three reasons for using modularity in this study. First, this measure can capture not only the extent of network segregation but also its global structure. This is because calculating the modularity involves searching for community assignments in the network. Although other representative measures of network segregation, such as global efficiency and transitivity, are helpful in confirming the robustness of the results obtained through modularity analyses, they may not necessarily consider a network's overall structure. This is because these measures are calculated based on the average of the values defined for each node (i.e., the shortest path length or number of triangles) [50, 51], which may not fully account for the holistic organization of the network. Second, by examining the connection patterns of the modules, it is possible to identify two types of neurons that play hub-like roles in the integration and segregation of the modules. The connector hubs were associated with module

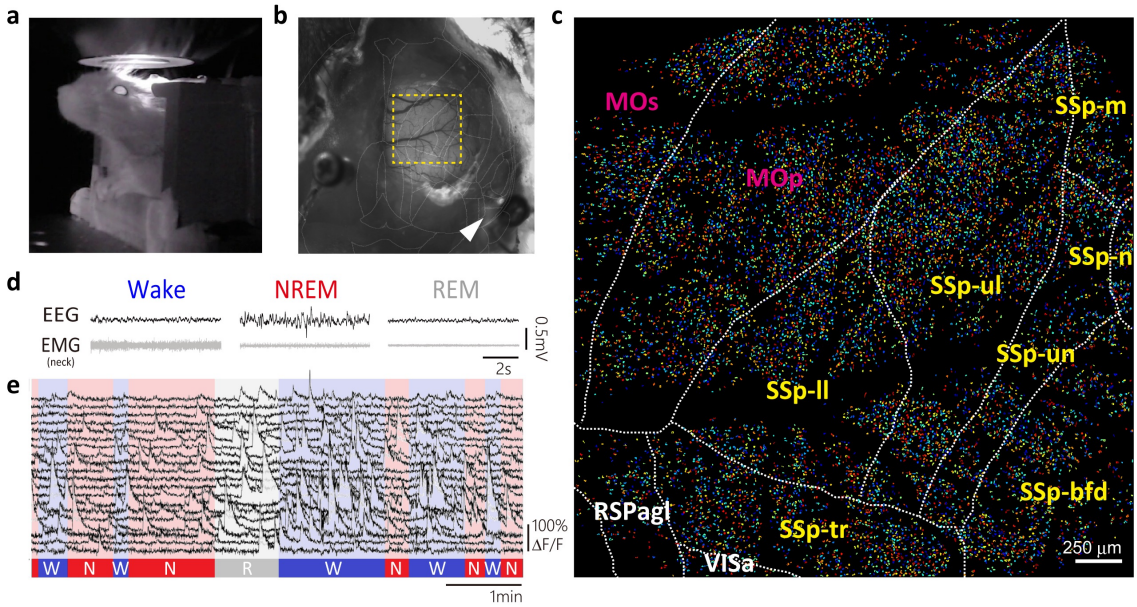

Figure 2: Fast, cell-resolution, wide-field two-photon calcium imaging from mice during wakefulness and sleep. **a.** An infrared camera image of a mouse under the FASHIO-2PM. **b.** A dorsal view of the mouse head. A yellow dashed square indicates the field-of-view (FOV). An arrowhead indicates a screw to acquire EEG from the same hemisphere on the imaging side. Overlaid white lines show borders according to the Allen Mouse Common Coordinate Framework. **c.** Activity of $>$ 10,000 neurons was recorded from a 3 mm $\times$ 3 mm FOV that included multiple brain regions. Borders between the regions are shown as white dashed lines according to the Allen Mouse Common Coordinate Framework. **d.** Examples of EEG and EMG recordings during the imaging session. The sleep-wake state was estimated by post-hoc analysis of EEG and EMG (see Materials and Methods). **e.** Representative Ca^{2+} signals from 20 randomly selected neurons are shown in sleep-wake states. The bottom color bar indicates the sleep-wake state of the mouse: wakefulness (W, blue), NREM (N, red), and REM sleep (R, gray). MOp, primary motor; MOs, secondary motor; SSp-bfd, S1-barrel field; SSp-ll, S1-lower limb, SSp-m, S1-mouse; SSp-n, S1-nose; SSp-tr, S1-trunk; SSp-ul, S1-upper limb; SSp-un, S1-unassigned area; RSPagl, retrosplenial area, lateral agranular part.

integration, whereas the provincial hubs were associated with module segregation (Fig. 1). In this study, we investigated the differences in the organization of functional networks between wakefulness and NREM sleep from these perspectives. Third, modularity can be computed even for large-scale networks, as analyzed in this study.

The degree of network integration during wakefulness and NREM sleep

To compare the modularity during wakefulness and NREM sleep, we estimated the functional networks. We calculated the Pearson correlation coefficients of the denoised $\Delta F/F$ between all node pairs (i.e., neuron pairs) with a window length of 196 s (see Materials and Methods). We then binarized the correlation matrices at a threshold set such that the connection density was equal to a certain value, K (Fig. 3a) [52]. This procedure prevented network measures from being trivially different because of variations in the number of links rather than in the pattern of connections (see Supplementary Fig. 2 for the relationship between connection density and absolute correlation threshold during wakefulness and NREM sleep). To demonstrate the robustness of the results across a wide range of K, we varied K from 0.008 to 0.3, which we considered as the lowest and highest values, respectively, for valid network analyses. When K was 0.008, the threshold absolute correlation value in some mice exceeded 0.65, which could have led to the absence of edges in highly correlated neuron pairs. Additionally, in some networks, the number of nodes in the largest connected component was less than 80% of the total number of nodes. Thus, for $K \leqq 0.008$, we consider the networks unsuitable for graph-theoretic analyses. When K was 0.3, the threshold absolute correlation value in some mice was below 0.08, which can lead to the presence of edges between non-significantly correlated neuron pairs. Thus, for $K \geqq 0.3$, we consider the networks unsuitable for graph-theoretic analyses.

To compute the modularity of the estimated functional networks, we first identified a module assignment that maximized the modularity index Q in Eq. (1), using the Louvain algorithm (Fig. 3a). The number of detected modules was not significantly different between wakefulness and NREM sleep when K was larger than 0.01, but it was larger during NREM sleep than during wakefulness only when K was 0.008 or 0.01 (Supplementary Fig. 3). After module assignment, we computed the modularity using Eq. (1).

We found that modularity was higher during NREM sleep than during wakefulness across different connection densities, except for the sparsest values, 0.008 and 0.01 (for connection density $K = 0.05$, $t = -3.9885$, 95% confidence interval of values during wakefulness minus NREM sleep: $(-0.0918, -0.0164)$; Fig. 3b; see also Supplementary Fig. 4 for other values of K). This suggests that functional cortical networks during NREM sleep are more segregated into modules than those during wakefulness. This difference could not be explained by the number of modules, as the number of modules was not significantly different between wakefulness and NREM sleep at most connection densities (Supplementary Fig. 3). Furthermore, when we set the number of modules to be the same (see Materials and Methods), similar results were obtained (Supplementary Fig. 5).

In addition to modularity, which considers the global structure of a network, we investigated whether other measures that do not necessarily consider such a structure had similar tendencies. The most basic and widely used measures are global efficiency and transitivity. We found that global efficiency was higher during wakefulness when K was sparser than 0.1 (Supplementary Fig. 6), and transitivity was higher during NREM sleep across different connection densities (Supplementary Fig. 7). These results suggest that functional networks are more segregated during NREM sleep than during wakefulness. The similar tendencies of global efficiency and transitivity and modularity indicate the robustness of the modularity results. From the next section, to understand detailed network structure at the single-cell-level, we focus on modularity and how modules are spatially distributed on the cortex.

Spatial distribution of modules

In the previous section, we found that functional networks were more segregated during NREM sleep than during wakefulness; however, whether this segregation occurs in a spatially localized manner

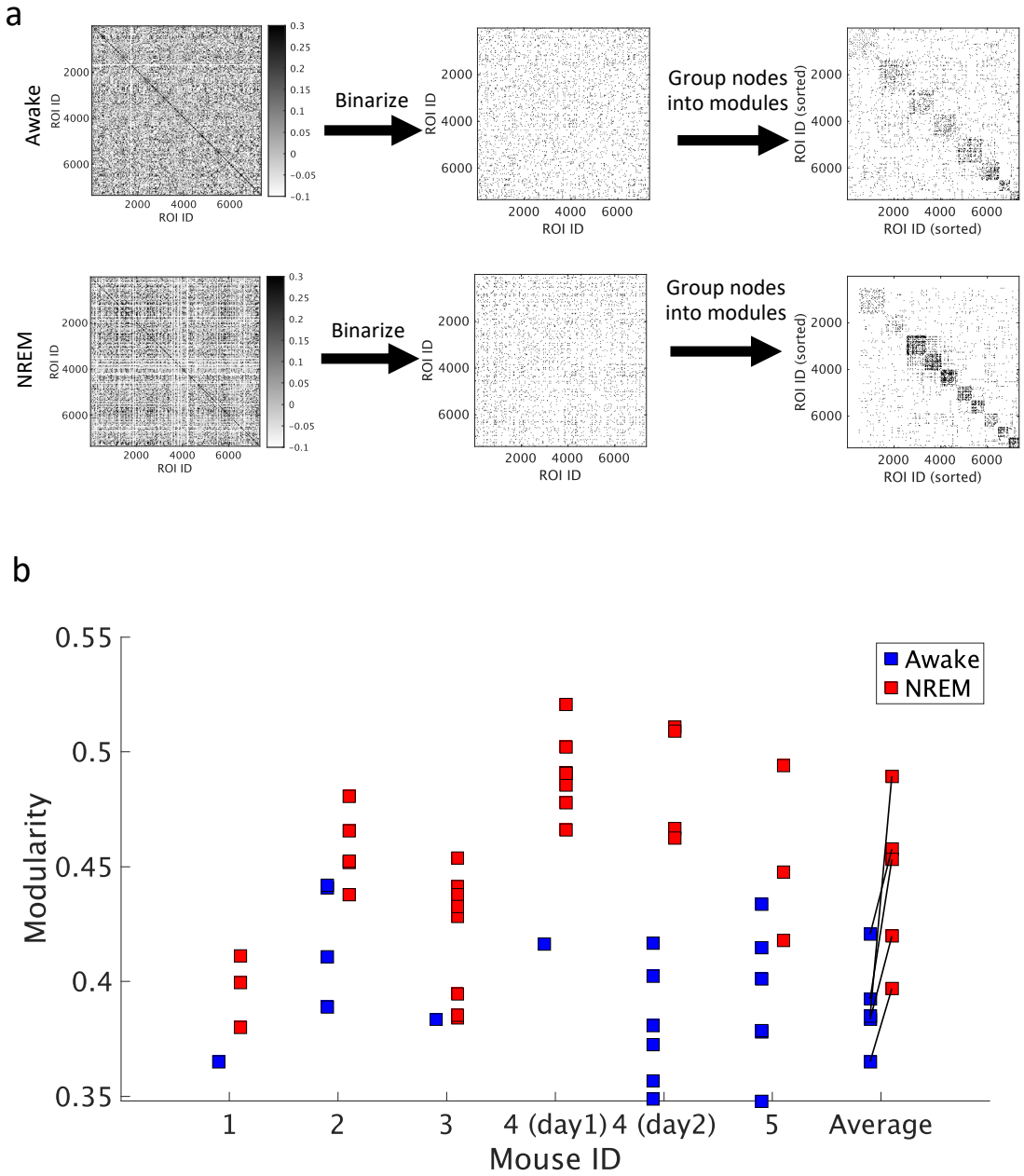

Figure 3: Estimation of functional networks and modularity. **a.** Procedures for estimating functional networks and calculating modularity. **b.** Comparison of modularity between wakefulness (blue squares) and NREM sleep (red squares) (connection density $K = 0.05$, $t = -3.9885$, 95% confidence interval of values during wakefulness minus NREM sleep: $(-0.0918, -0.0164)$). Each square for each mouse represents the value of modularity for each network, which was estimated using a non-overlapping 196-s window (1500 frames). Data from the same mouse are connected by black lines. For other values of K, see Supplementary Fig. 4.

remains unclear. To examine whether certain modules were confined to specific regions or scattered across regions, we examined their spatial distribution.

The modules were evenly spatially distributed during both wakefulness and NREM sleep (Fig. 4a, b). We did not observe particular modules localized in certain anatomical regions (Fig. 2c). This indicates that adjacent neurons do not necessarily belong to the same module, while distant neurons sometimes belong to the same module (Fig. 4a, b). Thus, even during NREM sleep, when functional networks are "segregated," long-range functional connections remain across brain regions. This spatial distribution was consistent between wakefulness and NREM sleep, although the degree of segregation differed between the two states.

To further clarify that the modules were almost spatially uniformly distributed, we examined whether there was a spatial imbalance in the composition of the modules. Specifically, we compared the composition of the modules within partial FOVs and the entire FOV. A comparison between a partial FOV and the entire FOV during wakefulness and NREM sleep is shown in Fig. 4a middle and 4b middle, respectively. We observed that the module composition was similar between the partial and entire FOVs. The correlations of the module proportions between the partial and entire FOV were 0.80 and 0.77 for wakefulness and NREM sleep, respectively. We also found that the activity patterns of neurons belonging to each module of the partial FOV were similar to those observed when viewing the entire FOV (Fig. 4a right, 4b right). This similarity in module composition was also observed between the other partial FOVs and the entire FOV. The correlation of the module proportion between the partial FOVs and the entire FOV was, on average, higher than 0.75 across all mice during both wakefulness and NREM sleep (see Supplementary Fig. 8). These results suggest that there is little spatial imbalance in the composition of the modules.

Two types of hub neurons

We identified two types of hub neurons related to module integration and segregation [45, 46] and investigated the spatial distribution of these hubs. While examining modularity provides information on the overall integration and segregation of a network, investigating hubs allows us to understand how individual neurons are involved in network segregation and integration. These two types of neurons are referred to as connector and provincial hubs (Fig. 1). Connector hubs have diverse inter-module connections, facilitating module integration, whereas provincial hubs have many within-module connections, facilitating module segregation. Two graph-theoretic measures, the participation coefficient and the within-module degree z-score, have been extensively used to successfully characterize these hubs (see Materials and Methods) [45, 46]. The participation coefficient quantifies the diversity of a node's connections across modules. It ranges from 0 to 1, where a value close to 1 indicates that the node has connections distributed evenly across multiple modules. The within-module degree z-score is the z-score of the within-module degree of a node. Although there are some variations in the specific criteria for defining connector and provincial hubs [6, 14, 16], we followed the definition given by Rubinov et al. [6], who defined nodes with high participation coefficients as connector hubs and nodes with high within-module degrees but low participation coefficients as provincial hubs. Specifically, we defined connector hubs as neurons with the top 10% participation coefficients and provincial hubs as neurons, excluding connector hubs, with within-module degree z-scores in the top 10% of all neurons. We illustrate in Fig. 5a-c how these hubs are connected in representative networks during wakefulness and NREM sleep.

The first step before examining the distribution of hubs was comparing the histogram of the participation coefficient between wakefulness and NREM sleep. This allowed us to understand how much the "connector hubness" of neurons differs between these states. Second we sought to understand how individual single neurons are involved in network segregation and integration. We explored possible differences in the spatial distributions of hubs during wakefulness and NREM sleep, and whether these hubs were scattered across regions similar to the distribution of modules or localized in specific regions.

First, we found that the participation coefficient was, on average, higher during wakefulness than during NREM sleep when K was less than or equal to 0.1 (Supplementary Fig. 9; see also Supplemen-

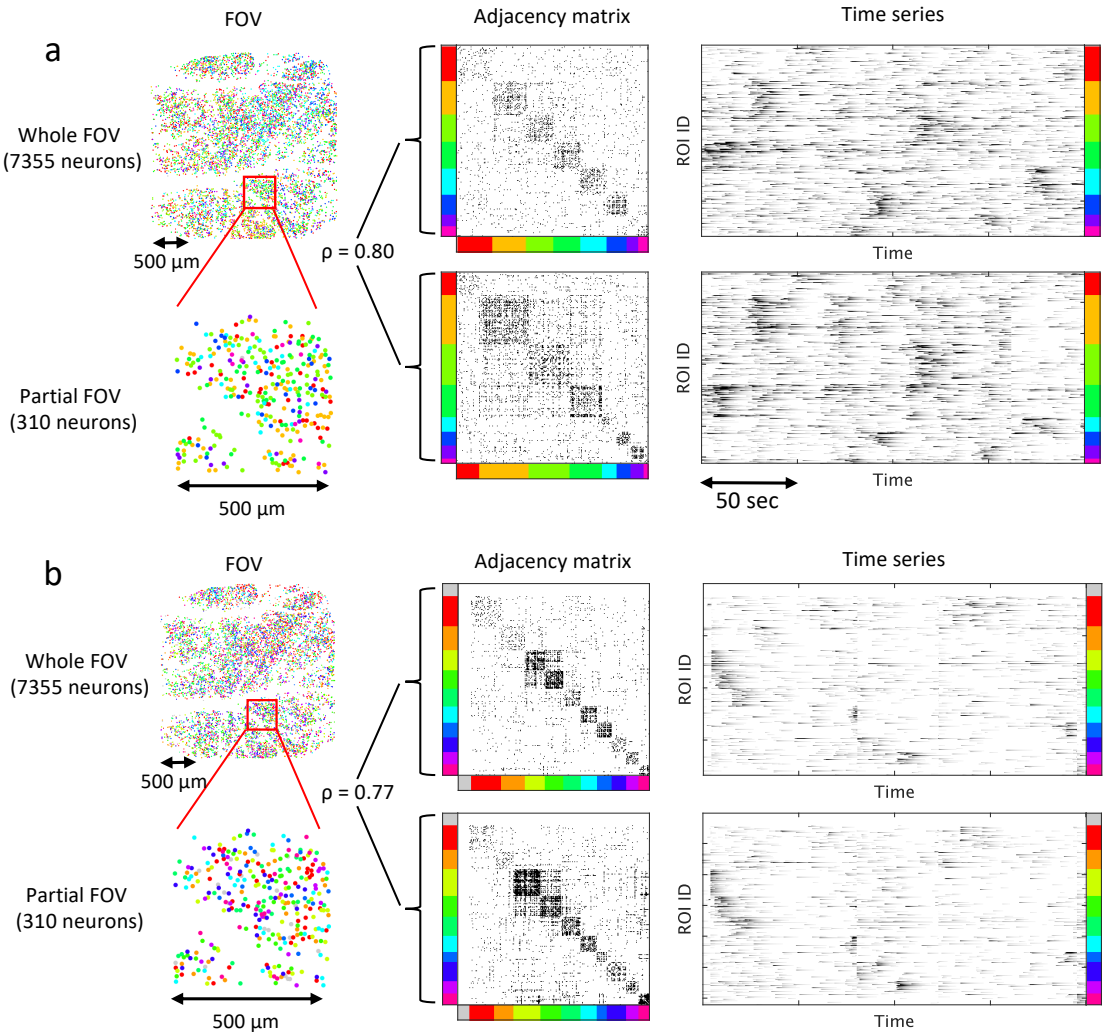

Figure 4: The spatial distribution of modules (left), adjacency matrix (middle), and time series (right) for both the entire FOV (top) and the partial FOV (bottom) of representative functional networks ($K = 0.05$) during wakefulness (**a**) and NREM sleep (**b**). Neurons within the adjacency matrices and time series are sorted based on their respective modules. Each distinct color represents a specific module. The gray-colored module consists of neurons that do not belong to the largest connected components of the network.

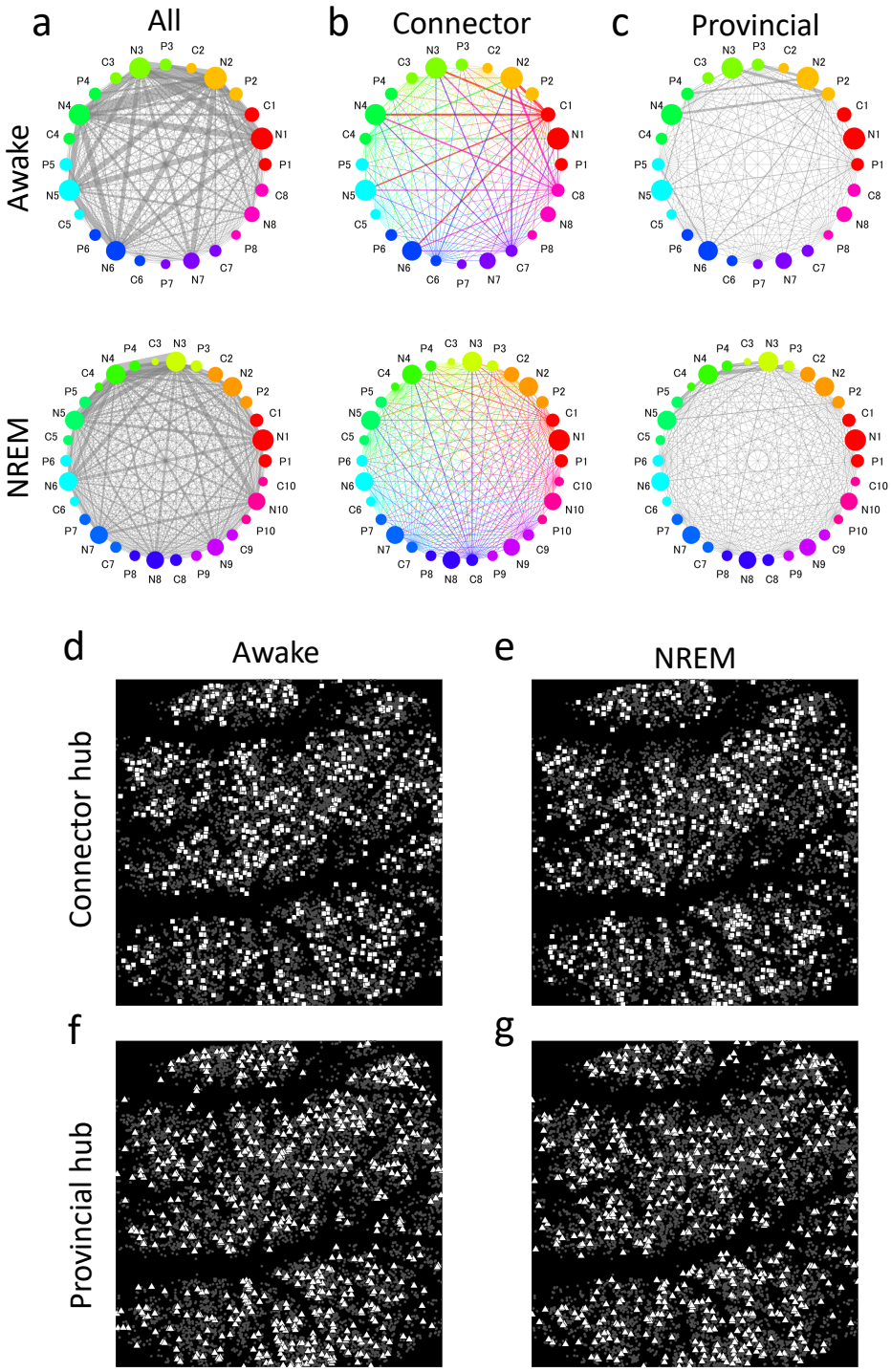

Figure 5: Connector and provincial hubs during wakefulness and NREM sleep. **a–c.** Representative visualization of functional networks during wakefulness and NREM sleep ($K = 0.05$). Colored circles represent connector hubs (C), provincial hubs (P), and non-hubs (N). The circle size represents the number of neurons, while the color of circles represents a module. Gray lines depict edges. The line width represents the number of edges. **a.** All edges are shown. **b.** Only the edges connected to connector hubs are shown. The edge color represents a module to which the connector hub that is linked to the edge belongs. **c.** Only the edges connected to provincial hubs are shown. **d, e.** Representative distribution of connector hubs (white squares) during wakefulness (**d**) and NREM sleep (**e**). **f, g.** Representative distribution of provincial hubs (white triangles) during wakefulness (**f**) and NREM sleep (**g**).

tary Fig. 10 for histograms of the participation coefficients.) This suggests that functional networks are more integrated during wakefulness than during NREM sleep, which is consistent with the modularity results. Second, we found that the hubs were spatially scattered during both wakefulness and NREM sleep (Fig. 5d–g), although the distribution was not necessarily completely uniform (Supplementary Figs. 11 and 12). This possibly suggests that functional networks are organized in a spatially scattered manner.

Distribution of coarse-grained modules

In an earlier section, we found that the modules were spatially scattered across regions. This contrasts with the known results for macro/mesoscale functional networks from EEG and fMRI studies, where the modules are spatially localized [14, 19, 25, 53]. To bridge this gap between the cellular and macro/mesoscales, we spatially coarse-grained cellular-scale calcium fluorescence signals at the mesoscale and examined how the module distribution changed (Fig. 6a). First, we divided the neurons into 100 parcels, each containing nearby cells. We then averaged the fluorescence signals per parcel and calculated the Pearson's correlation. The resulting correlation matrices were binarized to form networks, each comprising 100 nodes. We set the connection density threshold, K to 0.3 and identified the modules as described in the previous section.

The modules were localized during both wakefulness and NREM sleep in the coarse-grained networks (Fig. 6b). In other words, unlike cellular-resolution networks (Fig. 6c), nearby parcels are more likely to belong to the same modules than distant ones (Fig. 6d). These findings are in line with the module localization in macro/mesoscale EEG and fMRI networks. However, unlike these macro/mesoscale networks, we did not find a difference in the modularity between wakefulness and NREM sleep (Supplementary Fig. 13. See the Discussion for the parallels and differences between coarse-grained and macro/mesoscale networks.)

Thus, coarse graining drastically shifted the module distribution from scattered to localized; however, this raises the question of how this shift occurred. One possible explanation is that the correlations between nearby cells were slightly stronger than those between distant cells (but only to the extent that the module distribution was not localized at the cellular-scale). If this were the case, as correlations build up through coarse graining, the correlations between nearby parcels would become markedly higher than those between distant parcels, leading to module localization. To determine whether this was indeed the case, we investigated how the correlation depended on the distance and how the dependence changed as the level of coarse graining increased (see Materials and Methods).

First, for the case of no coarse graining, we found a subtle dependence of the correlation on distance for both wakefulness (Figs. 6e and 6g blue) and NREM sleep (Figs. 6f and 6g red) (Supplementary Fig. 13). However, this dependence was so minimal that the distribution of the correlation values remained largely unaffected by distance, which explains the scattering of modules in cellular-resolution networks. Contrastingly, as the level of coarse graining increased, the dependence became more intense for both wakefulness (Figs. 6e and 6g blue) and NREM sleep (Figs. 6f and 6g red) due to the buildup of weak activity correlations at the cellular level. This intensified dependence accounts for the module localization in coarse-grained networks.

Discussion

In this study, we recorded the spontaneous activities of approximately 5,000 to 10,000 neurons in a contiguous 3 mm $\times$ 3 mm FOV, including multiple cortices in each mouse (Fig. 2) and compared functional networks during wakefulness and NREM sleep (Fig. 1). We found that the functional networks during NREM sleep exhibited higher modularity (Fig. 3b; Supplementary Fig. 4), lower global efficiency (Supplementary Fig. 6), and higher transitivity (Supplementary Fig. 7) than those during wakefulness. These results suggest that functional networks during NREM sleep are more segregated than those during wakefulness. However, we found that the modules identified for the

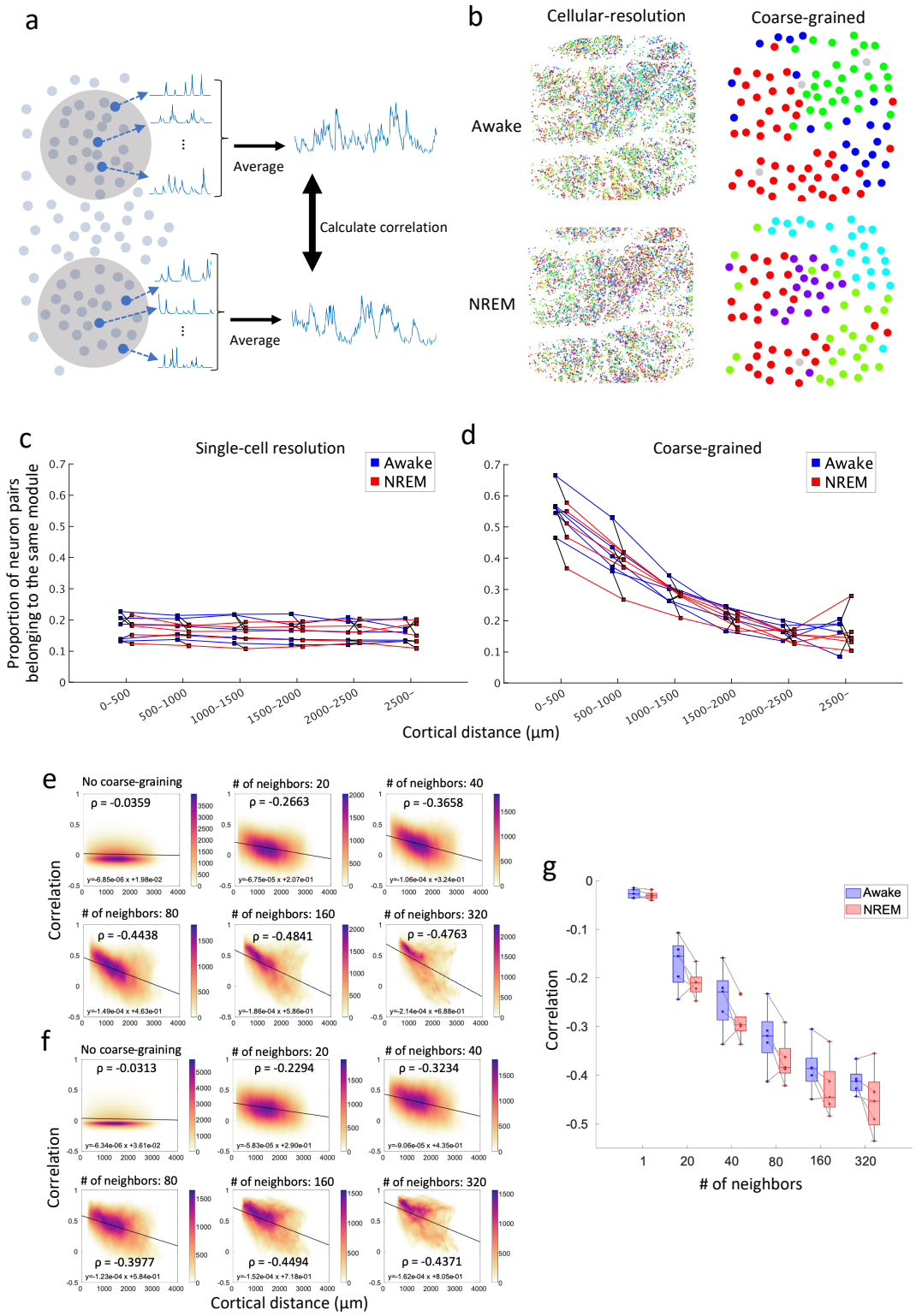

Figure 6: Distribution of coarse-grained modules. **a.** Schematics of coarse-grained functional network estimation. **b.** Example of the spatial distribution of cellular-resolution ($K = 0.05$) and coarse-grained ($K = 0.3$) modules. Each distinct color represents a specific module. The gray-colored module consists of neurons that do not belong to the largest connected components of the network. **c, d.** Relationships between cortical distances and module assignments of single-cell resolution functional networks ($K = 0.05$) (**c**) and coarse-grained functional networks ($K = 0.3$) (**d**) during wakefulness

Figure 6: (blue) and NREM sleep (red). The x-axis represents the cortical distance and the y-axis represents the proportion of neuron pairs belonging to the same modules. To match the sample size used in (**d**), the calculation in (**c**) was performed using 100 randomly sampled neurons. Values are averaged within each mouse. Data from the same mouse is connected with lines. **e, f.** Representative relationships between the cortical distances and the activity correlations at different levels of coarse graining (number of neighboring neurons per coarse-grained parcel = 1, 20, 40, 80, 160, and 320) are shown as density scatter plots. The number ρ is the correlation between the cortical distance and activity correlation. The solid lines represent the linear regression. (**e**) for wakefulness and (**f**) for NREM sleep. **g.** Correlation between cortical distances and activity correlations during wakefulness (blue) and NREM sleep (red). Each dot represents a mouse. Values are averaged within each mouse.

modularity calculations were spatially intermingled, that is, nearby neurons did not necessarily belong to the same module, and distant neurons sometimes did (Fig. 4; Fig. 6c). We also found that hubs were distributed across regions, although their distribution was not completely uniform (Fig. 5d, e; Supplementary Figs. 11–12). These results imply that functional networks are organized in a spatially intermixed manner. Additionally, we found that unlike cellular-resolution functional networks, modules of coarse-grained mesoscale functional networks were spatially localized (Fig. 6b right, 6d), potentially filling the gap between the structure of cellular-scale and macro/mesoscale functional networks.

In summary, our cellular-resolution and wide-FOV two-photon calcium imaging revealed that functional networks during NREM sleep are segregated more into modules during NREM sleep than during wakefulness (Fig. 3b; Supplementary Fig. 4), yet the modules are scattered in a mixed manner (Fig. 4; Fig. 6c), implying that there are functional connections across brain regions even during NREM sleep. Our findings offer new perspectives on variations in the organization of functional networks at the cellular level in different states of consciousness.

Neural mechanisms underlying spatially intermixed modules

In this section, we discuss the neural mechanisms underlying spatially intermixed modules (Fig. 4; Fig. 6c). Spatially intermixed modules imply that nearby neurons are not necessarily functionally connected, that is, they are not necessarily correlated, whereas distant neurons sometimes are. While we did find that nearby neurons are slightly more likely to be correlated than distant neurons (Fig. 6e, g), which can be explained by local synaptic connections [54–56], it is unclear why the observed trend is relatively weak, or equivalently, why the modules are spatially intermingled.

There are two possible explanations for this phenomenon: common inputs and indirect polysynaptic inputs. First, if there are common inputs to distant neurons and such common inputs do not depend much on the distance between the neurons, we would observe spatially scattered modules. Consistent with this, recent empirical evidence from anterograde tracing methods has shown that the projections of individual neurons are more diverse and divergent than previously indicated [57]. Second, in addition to common inputs, indirect polysynaptic inputs may explain these results. Because of the sampling rate of the recording and the slow kinetics of the Ca^{2+} sensor, we could not distinguish the correlations induced by monosynaptic direct inputs from those induced by polysynaptic direct inputs. Although correlations induced by monosynaptic direct inputs are strongly influenced by the distances between neurons, correlations induced by indirect polysynaptic direct inputs may not necessarily be strongly dependent on the distances, but rather depend on global circuit properties. As correlations in Ca^{2+} imaging are combinations of correlations induced by both monosynaptic and polysynaptic inputs, it is possible to empirically observe spatially scattered modules.

To further clarify the underlying neural mechanisms of spatially intermixed modules, a direct causality analysis, instead of the correlation analysis employed in this study, is needed. For example, perturbative approaches, such as optogenetic stimulation during imaging, can help assess the existence of causal interactions through direct synaptic connections [58, 59]. This step towards elucidating causal

relationships may offer deeper insights into the intricate mechanisms that shape spatially intermixed modules.

Comparison with previous studies on functional brain networks

In this section, we compare previous studies on network analysis of macro/mesoscale functional networks to explore their similarities and differences with single-cell resolution functional networks. It is important to note that there are various differences not only in the spatial scale (whether micro or macro), but also in the nature and properties of the signals being measured, measurement range, and experimental animals, to name a few. Therefore, a simple comparison cannot be made. We need to be aware of these differences.

Despite these limitations, some results reported in previous studies on human fMRI data are qualitatively similar to our findings. For example, human functional brain networks exhibit higher modularity during stage 2–4 of NREM sleep than during wakefulness [9, 14]. Additionally, they exhibit a higher global efficiency during wakefulness than during stage 1 NREM sleep [15]. These results are similar to our findings, suggesting that functional networks are more segregated during NREM sleep than during wakefulness.

However, we should note that the similarity could simply be a coincidence, as there is no theoretical guarantee that microscale functional networks (e.g., those observed in Ca^{2+} imaging) will have network properties similar to those of macroscale networks (e.g., those observed in fMRI). In fact, we also observed several differences. The differences in the spatial distribution of the modules are especially important. In the single-cell resolution functional networks examined in this study, the identified modules were spatially intermingled (Fig. 4; Fig. 6c), whereas in macro/mesoscale functional networks, they exhibit spatial localization [14, 19, 25, 53]. Additionally, in the mesoscale functional networks obtained from the coarse-grained calcium signals, we did not observe a difference in modularity between wakefulness and NREM sleep (Supplementary Fig. 13). Because these discrepancies are likely caused by various combined factors, such as differences in the measurement scale or properties of the measured signals, it is difficult to identify the main reason(s). We believe that the differences in network characteristics between sleep and wakefulness should continue to be investigated at both the micro and macroscale to obtain a more comprehensive system-level understanding of the neural mechanisms of sleep.

Two perspectives of the functional organization of the brain

In this section, we discuss two different perspectives of brain network organization, namely the localistic and holistic views. The former viewpoint posits that the brain is parceled into localized regions and that each region is responsible for specific information processing. For example, many functional network studies have reported that brain networks are segregated into spatially localized modules [14, 19, 25, 53, 60] that are thought to represent groups of nodes that perform similar brain functions and are responsible for specialized information processing [49]. This view is consistent with the theory of brain function localization [61, 62]. On the other hand, the latter viewpoint posits that cortical information processing is highly distributed; that is, the brain is not as neatly parceled into localized regions, as shown in the brain atlas. For example, we have previously reported that accurate somatosensory perception [63], perceptual memory consolidation [64], and memory enhancement [65] require coordinated activity in the primary somatosensory and secondary motor cortices. It has also been reported that behavior-related signals are represented brain-wide across species [66], including mice [67–69], flies [70], and worms [71]. These results suggest that the brain functions in a more distributed manner by coordinating different regions as a whole, which is consistent with the holism of brain function viewpoint [66, 72].

Our single-cell level network analysis (Fig. 4; Fig. 6c) supports the holistic perspective while our coarse-grained module analysis (Fig. 6b right, 6d) supports the localistic one. The significance of our study is that our analysis supports both views, depending on the activity resolution (i.e.,

macro/meso vs. micro). Therefore, our results may provide new insights that can bridge the gap between the two perspectives, namely that brain functions are macro/mesoscopically localized and microscopically globalized in the cortex. Such findings can only be obtained using single-cell resolution neural recordings across multimodal brain regions.

Materials and Methods

Animals

All animal experiments were performed in accordance with institutional guidelines and approved by the Animal Experiment Committee at RIKEN. Wild-type mice (C57BL/6JJmsSlc; Japan SLC, Shizuoka, Japan) were used. Male and female mice (12–24 weeks old) were used in this study. In all the experiments, the mice were housed in a 12 h-light/12 h-dark light cycle environment with *ad libitum* access to food and water.

Adeno-associated virus (AAV) vector preparation

G-CaMP7.09 [73] was subcloned into the synapsin I (SynI)-expressing vector from the pN1-G-CaMP7.09 vector construct. The AAV AAV-DJ-Syn-G-CaMP7.09-WPRE was produced as previously described [74].

Neonatal AAV injection and surgery

Neonatal AAV injections and surgery for two-photon imaging were performed using previously described protocols [43, 44] with slight modifications to the surgical procedure.

Neonatal mice (postnatal day 0–2) were collected from their cages and anesthetized on ice (cryoanesthesia) for 2–3 min before injection, and then mounted in a neonatal mouse head holder (custom-made, NARISHIGE). The AAV (diluted to 4.0×10^{12} GC/mL with 1 × phosphate buffer saline (PBS), 4 µL per pup) was injected into the neonatal cortex using a glass pipette (Q100-30-15, Sutter Instrument) with a diameter of 45–50 µm. The injection site was located at a depth of 250–300 µm in the frontal area. The injection procedure was completed within 10 min after cryoanesthesia initiation, and the pups were warmed until their body temperature returned to normal. After the pups began to move, they were returned to their mothers.

For surgery, mice (8–20 weeks) were anesthetized with isoflurane (2%). Once the mice failed to react to stimuli, we administered hypodermic injections of the combination agent [75]—Medetomidine/Midazolam/Butorphanol (MMB)—at a dose of 5 mL/kg body weight for the procedure. The MMB solution consisted of medetomidine (0.12 mg/kg body weight), midazolam (0.32 mg/kg body weight), butorphanol (0.4 mg/kg body weight), and saline. After anesthesia with MMB, the head was shaved and placed in head holders (SG-4N, NARISHIGE). During surgery, their body temperatures were maintained at 36–37°C using a feedback-controlled heat pad (BWT-100, Bio Research Center), and their eyes were coated with an ointment (Neo-Medrol EE Ointment, Pfizer Inc.). After removing the scalp, a 5-mm diameter cranitomy was performed over an area that included the primary somatosensory area of the right hemisphere. The craniotomy was then covered with a 5-mm diameter No.1 cover glass (Matsunami Glass Ind.) and sealed with dental cement (Super Bond, Sun Medical). After cranial window implantation, EEG and EMG were performed as described in previous reports [64, 76, 77]. Briefly, an EEG screw was implanted over the V2L region in the right hemisphere and over the parietal cortex in the left hemisphere and locked with dental cement. Separate EEG signals were referenced to the screws located in the cerebellar cortex. For the EMG recording, a flexible wire cable was implanted into the neck muscle. A stainless-steel headplate (custom-made, ExPP Co., Ltd.) was then cemented on the skull over the cerebellum as parallel to the window glass as possible. The exposed skull, EEG screws, and EMG wires were covered with dental cement. After surgery, the mice were treated with a

pesticidine-reversing agent, atipamezole hydrochloride (ANTISEDAN, Zoetis Inc.) solution at a dose of 0.12 mg/kg body weight. The mice were then placed on a heating pad to recover.

Skull images, including the cranial window of the head-fixed mouse, were acquired from one-photon macroscopic imaging after surgery to estimate the brain regions in the subsequent ROI analysis. The FOV was 13.3 mm $\times$ 13.3 mm and the image resolution was $1,024 \times 1,024$ pixels after $2\times$ spatial binning. The excitation light intensity from a blue LED source (LEX2-B-S, Brain Vision Inc.) and the gain and exposure time of the sCMOS camera (Zyla 5.5, Andor) were tuned so that none of the pixels were saturated.

In vivo two-photon calcium imaging of sleeping mice

In vivo two-photon imaging was performed using a custom-designed wide-field two-photon laser scanning microscope (FASHIO-2PM) [44]. To observe the spontaneous sleep-wake status in mice under the microscope, the mice were fixed in a custom-made stage box (ExPP Co., Ltd.) by firmly screwing the headplate to the stage, and then covered with an enclosure to maintain body temperature. The floor of the stage box was covered with the same bedding as that of the home cage. After recovery from surgery, the mice were head-fixed in a stage box daily during the light phase. The duration of head fixes increased daily from 1 min to 2 h in a steady manner to ensure that the head-fixed condition did not stress the mice. More than 2 weeks of habituation allowed the mice to show spontaneous wake/NREM/REM sleep states in the stage box. Before each imaging session, the imaging window was cleaned with a cotton swab soaked in acetone. The implanted EEG/EMG electrodes were connected to the connector. Fluorescence was observed in the somas of layer 2/3 neurons (120–150 µm below the surface). G-CaMP7.09 was excited at 920 nm using a tunable Ti:Sa laser (Maitai DeepSee, Spectra Physics) and the laser power was set to 60–80 mW at the front of the objective lens. The fluorescence of G-CaMP7.09 was detected with a GaAsP PMT in the range of 515–565 nm. All imaging sessions were performed for approximately 3–4 h/day at 7.65 frames/s with 2,048 $\times$ 2,048 pixels using custom-built software (Falcon, Nikon) and were saved as 16-bit monochrome tiff files.

EEG and EMG recording and analysis

EEG and EMG signals were recorded during the imaging experiments. EEG and EMG signals were amplified and filtered (EEG, 0.1–100 Hz; EMG, 5–300 Hz) using an analog amplifier (MEG-6116, NIHON KOHDEN). The signals were digitized using a 16-bit analog-to-digital converter (Digidata 1440A, Molecular Devices) at a sampling rate of 1 kHz and acquired using Clampex software (v. 10.7, Molecular Devices). To temporally match the EEG/EMG data with two-photon images, the scan-timing signals for two-photon imaging were digitized using the same system. Post-hoc sleep state determination was performed as previously described [64, 65]. EEG signals from the same hemisphere as the imaging were used for post-hoc analysis. Briefly, the root-mean-square (RMS) of EMG signals, EEG delta (1–4 Hz) power (normalized to power in 1–50 Hz), and theta (6–9 Hz) power (normalized to power in 1–4 Hz) were calculated in each 4-s sliding window, which is nearly equal to 30 frames of two-photon imaging. We defined brain states as follows: wakefulness, RMS value of EMG was above the threshold, which was defined manually in each animal; NREM, RMS value of EMG was below the threshold, and delta power/theta power was above 0.3; REM, the RMS value of the EMG was below the threshold, and the delta power/theta power was below 0.3. Sleep episodes of 12 s or less were dismissed and integrated into the sleep states before and after the episode. The transition from wakefulness to REM was considered a quiet wake.

Imaging data analysis

All the obtained images were first subjected to motion correction using NoRMCorre [78]. We then used a low-computational-cost cell-detection (LCCD) algorithm [79] to identify the ROIs corresponding to single neurons. The fluorescence time course $F_{ROI}(t)$ of each ROI was calculated by averaging all

pixels within the ROI, and the fluorescence signal of the cell body was estimated as $F(t) = F_{ROI} - r \times F_{neuropil}(t)$, where $r = 0.7$. The neuropil signal was defined as the average fluorescence intensity between 4 and 9 pixels from the boundary of the ROI (excluding all ROIs). The ΔF/F was calculated as $(F(t) - F_0(t))/F_0(t)$, where t is time and $F_0(t)$ is the baseline fluorescence estimated as the 8% percentile value of the fluorescence distribution collected in a ±30 s window around each sample time point [80]. The SNR of each ROI's ΔF/F was calculated using the "snr" function in MATLAB (MathWorks), where the signal was the ΔF/F below 0.5 Hz and the noise was the ΔF/F above 0.5 Hz. To exclude ROIs contaminated by noise, we selected ROIs that satisfied the following conditions: (1) The signal-to-noise ratio of ΔF/F was in the top 90%, (2) ROIs not obscured by nearby blood vessels, (3) the range of ΔF/F values fell between −1 and 10, (4) ROIs with at least one Ca^{2+} transient during recording, (5) the neuropil fluorescence was lower than that of the soma, (6) less than 45% of the frames had a ΔF/F lower than average, and (7) the correlation between ΔF/F and the square root of the EMG values was less than 0.2. Supplementary Table 1 shows the number of ROIs used in this study. We then denoised ΔF/F signals using OASIS [81], where we set the parameter smin to −2 and −3 when the signal-to-noise ratio was over and under 20, respectively. Subsequently, to cut off the tail end of the calcium fluorescence signal decay, we truncated ΔF/F values lower than 0.05.

All analyses to detect blood vessels were performed semi-automatically using ImageJ software [82] as follows. The median image of the two-photon images for 500 frames was converted into the frequency domain via a 2D Fourier transform. After extracting the low-frequency components of the image, an inverse Fourier transform was performed. Then, the blood vessel was detected by thresholding methods plugged in with ImageJ as function "AutoThreshold." The algorithm "MinError" was used for this.

Estimation of Functional Networks

To estimate the functional networks, we calculated the Pearson correlation coefficients of the denoised ΔF/F between all the neuron pairs with a window length of 196 s (1500 frames). Given that the sleep state of a mouse typically does not persist for more than 196 s, we segmented and combined the contiguous sections of equivalent states to achieve a cumulative duration of 196 s. We excluded frames with EMG potentials above a threshold in the previous and following 6.5 s (50 frames) to avoid motion-induced artifacts. We also excluded frames in which the same state (either wakefulness or NREM sleep) did not persist for more than 39 s (300 frames), to avoid ambiguity in determining whether the mouse was awake or asleep. We then binarized the correlation matrices at a threshold, setting it such that the ratio of the number of edges to all possible node pairs was equal to K [52]. For example, if $K = 0.01$, neuron pairs whose absolute correlation values rank in the top 1 percent are considered to have an edge. We varied K from 0.008 to 0.3 (from 0.008 to 0.01, 0.01 to 0.1, and 0.1 to 0.3 in 0.002, 0.01, and 0.05 increments, respectively).

Computation of confidence interval for the difference between wakefulness and NREM

To assess the statistically likely ranges of the differences in network measures between wakefulness and NREM sleep for each connection density K, confidence intervals were calculated for the difference. As the network measures were estimated multiple times using different time windows for each state within each mouse, the network measures were first averaged for each mouse and state. The average network measures of NREM sleep were subtracted from those of wakefulness for each mouse. Subsequently, the. 95% confidence interval of the difference in network measures between wakefulness and NREM sleep was computed based on a one-sample t-test with sample sizes of 5, with 4 degrees of freedom.

Graph Metrics

We calculated graph-theoretical measures using the Brain Connectivity Toolbox [6] and custom-made MATLAB codes.

Modularity Modularity is defined as the number of edges within modules minus the expected number of such edges [83],

$$Q = \frac{1}{2l} \sum_{ij} \left[A_{ij} - P_{ij} \right] \delta \left(g_i, g_j \right), \tag{1}$$

where l is the number of edges in the network, A_{ij} is an element of the adjacency matrix,

$$A_{ij} = \begin{cases} 1 & \text{if there is an edge between } i \text{ and } j \\ 0 & \text{otherwise,} \end{cases} \tag{2}$$

P_{ij} is the expected number of edges between i and j,

$$P_{ij} = \frac{k_i k_j}{2l}, \tag{3}$$

k_i is the degree of a node i, g_i is the module to which node i belongs, and $\delta(r, s)$ is defined as

$$\delta(r, s) = \begin{cases} 1 & \text{if } r = s \\ 0 & \text{otherwise.} \end{cases} \tag{4}$$

We identified a module assignment using the Louvain algorithm [84], which divides a network into modules to maximize Q, and then calculates the modularity. Because the Louvain algorithm is stochastic, we executed it 10 times for each network and chose a module assignment where the value of modularity was the largest. In the Louvain algorithm, the number of modules is automatically determined to maximize the modularity value. When we compared the modularity values by setting the number of modules, as shown in Supplementary Fig. 5, we set it to the smallest number of modules in the network that we wanted to compare. Iteration used the following process: selecting the two modules that resulted in the least decrease in modularity and then merging them.

Participation coefficient and within-module degree z-score Given a particular module assignment, we can calculate the participation coefficient and the within-module degree z-score of each node, allowing us to define connector and provincial hubs. The participation coefficient of node i is defined as [45][46]

$$y_i = 1 - \sum_{m \in M} \left(\frac{k_i(m)}{k_i} \right)^2, \tag{5}$$

where M is the set of modules and $k_i(m)$ is the number of edges between i and all nodes in module m. It quantifies the diversity of a node's connections across the modules. Therefore, a node with a high participation coefficient can be considered a connector hub [6]. In this study, we defined the neurons with the top 10 percent participation coefficients as connector hubs. The within-module z-score is defined as [45][46]

$$z_i = \frac{k_i \left(m_i \right) - \bar{k} \left(m_i \right)}{\sigma^{k(m_i)}}, \tag{6}$$

where m_i is the module to which node i belongs, and $\bar{k}(m_i)$ and $\sigma^{k(m_i)}$ are respectively mean and standard deviation of the within-module m_i degree distribution. It quantifies the number of edges that a node has within the module to which it belongs. Therefore, a node with a high within-module degree z-score but with a low participation coefficient can be considered a provincial hub [6]. We defined neurons, excluding connector hubs, with within-module degree z-scores in the top 10 percent of all neurons as provincial hubs.

Global efficiency and transitivity We also calculated the global efficiency and the transitivity as measures of network integration and segregation. The global efficiency is defined as the average inverse shortest path length,

$$E = \frac{1}{n} \sum_{i \in N} E_i = \frac{1}{n} \sum_{i \in N} \frac{\sum_{j \in N, j \neq i} d_{ij}^{-1}}{n-1}, \tag{7}$$

where N is the set of all nodes in the network, n is the number of nodes, and d_{ij} is the shortest path length between node i and j [50]. This measure quantifies how efficiently one node can communicate with another. The transitivity is defined as the fraction of triangles in a network,

$$T = \frac{\sum_{i \in N} 2t_i}{\sum_{i \in N} k_i (k_i - 1)}, \tag{8}$$

where t_i is the number of triangles around node i and k_i is the degree of node i [51]. A large number of triangles implies segregation.

Dependence of activity correlation on cortical distance

To examine the relationship between the cell activity correlation and cortical distance, we visualized this relationship using density scatter plots (top-left panels in Figs. 6e and 6f). We opted for density scatter plots over normal scatter plots (plotting individual points), because of the large number of cell pairs. We also calculated the correlation between activity correlation and distance and performed a least-squares linear regression analysis.

To evaluate the changes in this relationship at various coarse-grained levels, we

1. For each cell, i, selected its $(k-1)$ nearest neighbors and calculated the average activity across k cells, including cell i.

2. Calculated the average cortical coordinates for the k cells.

3. Compared the correlation between averaged activities with the distance between averaged coordinates using the same methods applied in the no coarse graining analysis described above. This involved visualization with density scatter plots, computing the correlation between activity and distance, and conducting linear regression. During these steps, pairs with overlapping neighboring cell sets were excluded.

4. Varied the number of neighbors, k, ranging from 20 to 320.

References

[1] Dehaene, S. & Changeux, J.-P. Experimental and theoretical approaches to conscious processing. Neuron **70**, 200–227 (2011).

[2] Mashour, G. A., Roelfsema, P., Changeux, J.-P. & Dehaene, S. Conscious processing and the global neuronal workspace hypothesis. Neuron **105**, 776–798 (2020).

[3] Oizumi, M., Albantakis, L. & Tononi, G. From the phenomenology to the mechanisms of consciousness: integrated information theory 3.0. PLoS Comput. Biol. (2014).

[4] Tononi, G., Boly, M., Massimini, M. & Koch, C. Integrated information theory: from consciousness to its physical substrate. Nat. Rev. Neurosci. **17**, 450–461 (2016).

[5] Deco, G., Tononi, G., Boly, M. & Kringelbach, M. L. Rethinking segregation and integration: contributions of whole-brain modelling. Nat. Rev. Neurosci. **16**, 430–439 (2015).

[6] Rubinov, M. & Sporns, O. Complex network measures of brain connectivity: uses and interpretations. Neuroimage **52**, 1059–1069 (2010).

[7] Seguin, C., Sporns, O. & Zalesky, A. Brain network communication: concepts, models and applications. Nat. Rev. Neurosci. (2023).

[8] Afrasiabi, M. et al. Consciousness depends on integration between parietal cortex, striatum, and thalamus. Cell Syst **12**, 363–373.e11 (2021).

[9] Boly, M. et al. Hierarchical clustering of brain activity during human nonrapid eye movement sleep. Proc. Natl. Acad. Sci. U. S. A. **109**, 5856–5861 (2012).

[10] Casali, A. G. et al. A theoretically based index of consciousness independent of sensory processing and behavior. Sci. Transl. Med. **5**, 198ra105 (2013).

[11] Lee, M. et al. Connectivity differences between consciousness and unconsciousness in non-rapid eye movement sleep: a TMS-EEG study. Sci. Rep. **9**, 5175 (2019).

[12] Massimini, M. et al. Breakdown of cortical effective connectivity during sleep. Science **309**, 2228–2232 (2005).

[13] Schartner, M. M. et al. Global and local complexity of intracranial EEG decreases during NREM sleep. Neurosci Conscious **2017**, niw022 (2017).

[14] Tagliazucchi, E. et al. Large-scale brain functional modularity is reflected in slow electroencephalographic rhythms across the human non-rapid eye movement sleep cycle. Neuroimage **70**, 327–339 (2013).

[15] Uehara, T. et al. Efficiency of a "small-world" brain network depends on consciousness level: a resting-state FMRI study. Cereb. Cortex **24**, 1529–1539 (2014).

[16] Bertolero, M. A., Yeo, B. T. T., Bassett, D. S. & D'Esposito, M. A mechanistic model of connector hubs, modularity and cognition. Nat Hum Behav **2**, 765–777 (2018).

[17] Bertolero, M. A., Yeo, B. T. T. & D'Esposito, M. The modular and integrative functional architecture of the human brain. Proc. Natl. Acad. Sci. U. S. A. **112**, E6798–807 (2015).

[18] Chavez, M., Valencia, M., Navarro, V., Latora, V. & Martinerie, J. Functional modularity of background activities in normal and epileptic brain networks. Phys. Rev. Lett. **104**, 118701 (2010).

[19] Cohen, J. R. & D'Esposito, M. The segregation and integration of distinct brain networks and their relationship to cognition. J. Neurosci. **36**, 12083–12094 (2016).

[20] Gordon, E. M. et al. Three distinct sets of connector hubs integrate human brain function. Cell Rep. **24**, 1687–1695.e4 (2018).

[21] Kim, H. et al. Estimating the integrated information measure phi from High-Density electroencephalography during states of consciousness in humans. Front. Hum. Neurosci. **12**, 42 (2018).

[22] Luppi, A. I. et al. Consciousness-specific dynamic interactions of brain integration and functional diversity. Nat. Commun. **10**, 4616 (2019).

[23] Luppi, A. I. et al. LSD alters dynamic integration and segregation in the human brain. Neuroimage **227**, 117653 (2021).

[24] Shine, J. M. et al. The dynamics of functional brain networks: Integrated network states during cognitive task performance. Neuron **92**, 544–554 (2016).

[25] Tagliazucchi, E. et al. Increased global functional connectivity correlates with LSD-Induced ego dissolution. Curr. Biol. **26**, 1043–1050 (2016).

[26] Yanagawa, T., Chao, Z. C., Hasegawa, N. & Fujii, N. Large-scale information flow in conscious and unconscious states: an ECoG study in monkeys. PLoS One **8**, e80845 (2013).

[27] Betzel, R. F. & Bassett, D. S. Multi-scale brain networks. Neuroimage **160**, 73–83 (2017).

[28] Sporns, O. Networks of the Brain (MIT Press, 2016).

[29] Shepherd, G. M. Foundations of the neuron doctrine (Oxford University Press, 2015).

[30] Ebitz, R. B. & Hayden, B. Y. The population doctrine in cognitive neuroscience. Neuron (2021).

[31] Yuste, R. From the neuron doctrine to neural networks. Nat. Rev. Neurosci. **16**, 487–497 (2015).

[32] Hoel, E. P., Albantakis, L. & Tononi, G. Quantifying causal emergence shows that macro can beat micro. Proc. Natl. Acad. Sci. U. S. A. **110**, 19790–19795 (2013).

[33] Northoff, G. & Huang, Z. How do the brain's time and space mediate consciousness and its different dimensions? temporo-spatial theory of consciousness (TTC). Neurosci. Biobehav. Rev. **80**, 630–645 (2017).

[34] Northoff, G., Wainio-Theberge, S. & Evers, K. Is temporo-spatial dynamics the "common currency" of brain and mind? in quest of "spatiotemporal neuroscience". Phys. Life Rev. **33**, 34–54 (2020).

[35] Betzel, R. F., Wood, K. C., Angeloni, C., Neimark Geffen, M. & Bassett, D. S. Stability of spontaneous, correlated activity in mouse auditory cortex. PLoS Comput. Biol. **15**, e1007360 (2019).

[36] Koçillari, L. et al. Measuring stimulus-related redundant and synergistic functional connectivity with single cell resolution in auditory cortex (2023).

[37] Miyazaki, T. et al. Dynamics of cortical local connectivity during Sleep–Wake states and the homeostatic process. Cereb. Cortex **30**, 3977–3990 (2020).

[38] Yang, W. et al. Anesthetics fragment hippocampal network activity, alter spine dynamics, and affect memory consolidation. PLoS Biol. **19**, e3001146 (2021).

[39] Yu, Y., Stirman, J. N., Dorsett, C. R. & Smith, S. L. Mesoscale correlation structure with single cell resolution during visual coding. BioRxiv (2019).

[40] Clawson, W. et al. Computing hubs in the hippocampus and cortex. Sci Adv **5**, eaax4843 (2019).

[41] Dann, B., Michaels, J. A., Schaffelhofer, S. & Scherberger, H. Uniting functional network topology and oscillations in the fronto-parietal single unit network of behaving primates. Elife **5** (2016).

[42] Nigam, S. et al. Rich-Club organization in effective connectivity among cortical neurons. J. Neurosci. **36**, 670–684 (2016).

[43] Oomoto, I. et al. Protocol for cortical-wide field-of-view two-photon imaging with quick neonatal adeno-associated virus injection. STAR Protoc **2**, 101007 (2021).

[44] Ota, K. et al. Fast, cell-resolution, contiguous-wide two-photon imaging to reveal functional network architectures across multi-modal cortical areas. Neuron **109**, 1810–1824.e9 (2021).

[45] Guimerà, R. & Amaral, L. A. N. Cartography of complex networks: modules and universal roles. J. Stat. Mech. **2005**, nihpa35573 (2005).

[46] Guimerà, R. & Nunes Amaral, L. A. Functional cartography of complex metabolic networks. Nature **433**, 895–900 (2005).

[47] Newman, M. E. J. Fast algorithm for detecting community structure in networks. Phys. Rev. E Stat. Nonlin. Soft Matter Phys. **69**, 066133 (2004).

[48] Newman, M. E. J. & Girvan, M. Finding and evaluating community structure in networks. Phys. Rev. E Stat. Nonlin. Soft Matter Phys. **69**, 026113 (2004).

[49] Sporns, O. & Betzel, R. F. Modular brain networks. Annu. Rev. Psychol. **67**, 613–640 (2016).

[50] Latora, V. & Marchiori, M. Efficient behavior of small-world networks. Phys. Rev. Lett. **87**, 198701 (2001).

[51] Newman, M. E. J. The structure and function of complex networks. SIAM Rev. **45**, 167–256 (2003).

[52] Bullmore, E. T. & Bassett, D. S. Brain graphs: graphical models of the human brain connectome. Annu. Rev. Clin. Psychol. **7**, 113–140 (2011).

[53] Muldoon, S. F., Soltesz, I. & Cossart, R. Spatially clustered neuronal assemblies comprise the microstructure of synchrony in chronically epileptic networks. Proceedings of the National Academy of Sciences **110**, 3567–3572 (2013).

[54] Douglas, R. J., Koch, C., Mahowald, M., Martin, K. A. & Suarez, H. H. Recurrent excitation in neocortical circuits. Science **269**, 981–985 (1995).

[55] Harris, K. D. & Mrsic-Flogel, T. D. Cortical connectivity and sensory coding. Nature **503**, 51–58 (2013).

[56] Ko, H. et al. Functional specificity of local synaptic connections in neocortical networks. Nature **473**, 87–91 (2011).

[57] Han, Y. et al. The logic of single-cell projections from visual cortex. Nature **556**, 51–56 (2018).

[58] Fişek, M. et al. Cortico-cortical feedback engages active dendrites in visual cortex. Nature (2023).

[59] Izquierdo-Serra, M., Hirtz, J. J., Shababo, B. & Yuste, R. Two-Photon optogenetic mapping of excitatory synaptic connectivity and strength. iScience **8**, 15–28 (2018).

[60] Betzel, R. F. Organizing principles of whole-brain functional connectivity in zebrafish larvae. Netw Neurosci **4**, 234–256 (2020).

[61] Herbet, G. & Duffau, H. Revisiting the functional anatomy of the human brain: Toward a Meta-Networking theory of cerebral functions. Physiol. Rev. **100**, 1181–1228 (2020).

[62] Posner, M. I., Petersen, S. E., Fox, P. T. & Raichle, M. E. Localization of cognitive operations in the human brain. Science **240**, 1627–1631 (1988).

[63] Manita, S. et al. A Top-Down cortical circuit for accurate sensory perception. Neuron **86**, 1304–1316 (2015).

[64] Miyamoto, D. et al. Top-down cortical input during NREM sleep consolidates perceptual memory. Science **352**, 1315–1318 (2016).

[65] Saito, Y. et al. Emotional association enhances perceptual memory through amygdalo-cortical inputs during NREM sleep (2023).

[66] Kaplan, H. S. & Zimmer, M. Brain-wide representations of ongoing behavior: a universal principle? Curr. Opin. Neurobiol. **64**, 60–69 (2020).

[67] Musall, S., Kaufman, M. T., Juavinett, A. L., Gluf, S. & Churchland, A. K. Single-trial neural dynamics are dominated by richly varied movements. Nat. Neurosci. **22**, 1677–1686 (2019).

[68] Salkoff, D. B., Zagha, E., McCarthy, E. & McCormick, D. A. Movement and performance explain widespread cortical activity in a visual detection task. Cereb. Cortex **30**, 421–437 (2020).

[69] Stringer, C. et al. Spontaneous behaviors drive multidimensional, brainwide activity. Science **364**, 255 (2019).

[70] Aimon, S. et al. Fast near-whole–brain imaging in adult drosophila during responses to stimuli and behavior. PLoS Biol. **17**, e2006732 (2019).

[71] Kato, S. et al. Global brain dynamics embed the motor command sequence of caenorhabditis elegans. Cell **163**, 656–669 (2015).

[72] Westlin, C. et al. Improving the study of brain-behavior relationships by revisiting basic assumptions. Trends Cogn. Sci. (2023).

[73] Shiba, Y. et al. Allogeneic transplantation of iPS cell-derived cardiomyocytes regenerates primate hearts. Nature **538**, 388–391 (2016).

[74] Kobayashi, K. et al. Survival of corticostriatal neurons by Rho/Rho-kinase signaling pathway. Neurosci. Lett. **630**, 45–52 (2016).

[75] Kawai, S., Takagi, Y., Kaneko, S. & Kurosawa, T. Effect of three types of mixed anesthetic agents alternate to ketamine in mice. Exp. Anim. **60**, 481–487 (2011).

[76] Tsunematsu, T. et al. Acute optogenetic silencing of orexin/hypocretin neurons induces slow-wave sleep in mice. J. Neurosci. **31**, 10529–10539 (2011).

[77] Tsunematsu, T. et al. Long-lasting silencing of orexin/hypocretin neurons using archaerhodopsin induces slow-wave sleep in mice. Behav. Brain Res. **255**, 64–74 (2013).

[78] Pnevmatikakis, E. A. & Giovannucci, A. NoRMCorre: An online algorithm for piecewise rigid motion correction of calcium imaging data. J. Neurosci. Methods **291**, 83–94 (2017).

[79] Ito, T. et al. Low computational-cost cell detection method for calcium imaging data. Neurosci. Res. **179**, 39–50 (2022).

[80] Dombeck, D. A., Khabbaz, A. N., Collman, F., Adelman, T. L. & Tank, D. W. Imaging large-scale neural activity with cellular resolution in awake, mobile mice. Neuron **56**, 43–57 (2007).

[81] Friedrich, J., Zhou, P. & Paninski, L. Fast online deconvolution of calcium imaging data. PLoS Comput. Biol. **13**, e1005423 (2017).

[82] Schneider, C. A., Rasband, W. S. & Eliceiri, K. W. NIH image to ImageJ: 25 years of image analysis. Nat. Methods **9**, 671–675 (2012).

[83] Newman, M. E. J. Modularity and community structure in networks. Proc. Natl. Acad. Sci. U. S. A. **103**, 8577–8582 (2006).

[84] Blondel, V. D., Guillaume, J. L., Lambiotte, R. & others. Fast unfolding of communities in large networks. Journal of statistical (2008).

Acknowledgements

We thank Ben Fulcher, Muneki Ikeda, and Yoshihito Saito for valuable comments and discussions. This research was supported by the Japan Society for the Promotion of Science (JSPS) KAKENHI Grant Numbers JP19J01973 to I.O., JP20H05775 to M.M, 20H05712 and 23H04834 to M.O., the AMED-Brain/Minds Project Grant Number JP15dm0207001 to M.M., KAO Corp. to M.M., the Toray Science Foundation to M.M., Japan Science and Technology Agency (JST) CREST Grant Number JPMJCR1864 to D.K., J.K., and M.O., and JST SPRING Grant Number JPMJSP2108 to D.K..